First principles insights into improved catalytic performance of $BaTiO_3$- graphene nanocomposites in conjugation with experimental investigations

Monisha Rastogi[a], *Chris Bowen*[b], *H.S. Kushwaha*[a], *Rahul Vaish*[a,c]*

[a]School of Engineering, Indian Institute of Technology Mandi, 175 001, India.

[b]Department of Mechanical Engineering, University of Bath, BA2 7AY, UK.

[c]Materials Research Centre, Indian Institute of Science, Bangalore 560 012, India

*Email:rahul@iitmandi.ac.in,Phone:+91-1905-237921,Fax:+91-1905-237945

Abstract

The present work aims to provide first principles insights into the catalytic performance of composites based on $BaTiO_3$ particles decorated over reduced graphene oxide (rGO).Examination regarding the orbital contributions of valence states, conduction states, interaction surface and anchoring of perovskite over rGO have been carried out. Theoretical results thus obtained have been validated using experimental investigation. Further experiments have also been conducted to analyze the catalytic performance of composites with respect to multiple advanced oxidation processes. Charge separation has been improved due to rGO acting as macromolecular photosensitizer. Degradation of xanthene dye (Rhodamine B) and methyl orange (MO) assisted in evaluation of the catalytic performance. Acoustic irradiation provides an additional route to improve degradation by ameliorating catalytic activity (from 0.036min to 0.099minin RhB especially). Synergistic effect obtained through conjugated benefits of oxidation processes with proposed composite, played a crucial role in improving the overall efficiency. The cumulative outcome of the results indicates superior performance of $BaTiO_3$-rGO composites for green and sustainable water treatment applications.

Keywords: *Advanced oxidation processes; first principles; barium titanate-rGO composite; dye degradation; water pollution; ferroelectric*

1. Introduction

Ferroelectric-perovskite based catalytic applications have recently attracted considerable advocacy owing to its promising applications in the field of environmental detoxification. This can be attributed to the presence of adequate cathodic conduction band (CB) energies and a recently reported stern layer formation[1]; which assists in effective electron-hole separation at the catalyst-medium interface. However, owing to the major shortcomings which includes low quantum yield under visible light irradiation and wide band gap, it is crucial to tailor its properties to enable practical applications[2-5].

In this context, composite of $BaTiO_3$ (promising ferroelectric perovskite) with reduced graphene oxide (rGO) has been considered in this work. rGO has been used owing to several merits such as high adsorption capacity, enhanced surface area and increased porosity[6, 7]. Further, the photoexcited state of rGO acted as an electron donor for perovskite, facilitating injection of these electrons into its conduction band. This is followed by subsequent radical reactions, therefore rGO acts as a macromolecular photosensitizer[8, 9].Though such composites have been investigated for photocatalytic applications[10-16], this is the first theoretical study that we are aware of, which clearly illustrates the phenomenon occurring at microscopic level. In addition, it assisted in elucidation of interactions, orbital contributions and nature of anchoring between perovskite particles and rGO.

Further, the performance of the proposed composite in the context of multiple advanced oxidation processes (AOPs) including photocatalysis, sonocatalysis and sonophotocatalysis has also been addressed experimentally. The hybrid approach of sonophotocatalysis[17]offered multiple advantages including enhanced mass transfer, de-agglomeration of catalyst and augmented turbulence of the aqueous medium. Xanthene dye (Rhodamine B, RhB) and azo dye (methyl orange, MO) have been selected in this work to evaluate the catalytic performance for various oxidation processes. It will be demonstrated

that degradation process involving a synergistic effect (employing benefits of multiple AOPs and $BaTiO_3$-rGO) results in higher degradation efficiency. Results indicate that the proposed approach addresses multiple shortcomings associated with traditional catalysts and could pave way for the future of sustainable water treatment.

2. Theoretical and Experimental Section

2.1. First principles investigations. CASTEP commercial package[18] has been employed to perform the first-principle DFT calculations using plane wave pseudo-potential formalism method. A local density approximation (LDA) approach has been used to perform computations coupled with Ceperley-Alders exchange correlation potential which was parameterized using the Perdew-Zunger scheme, without considering the spin polarization. The conjugated gradient technique has been employed in a direct minimization of Kohn-Sham energy functional, with pseudopotentials representing the core electrons in frozen form. The Monkhorst pack scheme generated the k points that accounted for crystal reciprocal lattices. The existing literature reveals that LDA underestimates the band gap for both semiconductors and insulators[19, 20]. Hence, a correction or scissor operator is often required to achieve the band gap that compliments the experimental investigations. For both systems, the energy cut off was 410 eV. Three-dimensional periodic boundary conditions have been employed for both pristine and the composite system. The vacuum space of 15Å at Z-axis while building the composite assisted in avoiding surface interaction, which otherwise could have interfered with the trajectories generating periodic images. Increasing the k-point set to higher value of 6 x 6 x 1 mesh enabled good agreement with reported results. However, a further increase in density of the k point grid did not alter the results significantly. Geometry optimization for the systems facilitated in relaxing all atoms to attain the most stable configuration for systems under consideration. Similar studies have been conducted for CdS by Jose *et. al.*[21] and Dong *et. al.*[22] and with TiO_2 cluster by Albaret *et.al*.[23] ,

Qu*et. al.*[24] and Geng *et. al*.[25]. Expanding upon the same approach, $BaTiO_3$ cluster (n=2) has been considered with 7 x 7 supercell of rGO. Figure 1 shows the optimized structure corresponding to $BaTiO_3$ cluster (n=2) decorated over rGO. As clearly reflected, all three possible isomers of $(BaTiO_3)_2$ clusters have been considered to approach the rGO sheets. After evaluation of binding energy for each of the system, it could be deduced that figure 1 (a) corresponds to the highest binging energy of 1.78 eV. Hence, this isomer corresponds to the most stable structure and has been considered for further calculations. The equilibrium distance between the rGO layer and the top of $BaTiO_3$ cluster is calculated to be 2.73 Å. The investigations have been performed considering the convergence threshold, energy and force to be $2x10^{-6}$ eV per atom, 2 x 10^{-5}eV and 0.05eVÅ^{-1} respectively. The projected density of states (PDOS) of the considered catalyst has been evaluated to elucidate the orbital contribution, direction of charge transfer and nature of electronic coupling.

2.2. Chemicals. $BaCO_3$ and TiO_2 powders (Alfa Aesar) were used to synthesize $BaTiO_3$ using conventional solid-oxide reaction route. Graphene oxide was prepared using modified Hummers' method[26]. The ferroelectric-rGO composites have been prepared using hydrothermal synthesis using hydrazine as a reducing agent. The starting raw materials, GO solution and $BaTiO_3$were subjected to continuous stirring for 1 hour, after mixing into their stoichiometric ratio, to obtain 10% rGO by weight, in the composite. Thereafter, the reaction mixture has been subjected to hydrothermal treatment for 3 hours at 200°C after transferring it to a Teflon autoclave. The obtained product was subjected to centrifugation for 10 minutes at 4000 rpm. The centrifuged product was further washed and dried to obtain $BaTiO_3$ – rGO composites.

2.3. Characterization techniques. The phase homogeneity and purity of the fabricated samples was analyzed using automated powder X-ray powder diffraction on a RIGAKU-9kW rotating anode with Cu-Kα source. A scan rate of 0.02˚/s over the 2θ range of 20˚ to 80˚has

been used. Scanning electron microscope (SEM) (FESEM, Inspect™S50) has been employed to evaluate surface morphology, microstructure, particle size and composition of the samples. Energy-dispersive X-ray (EDX) spectroscopy enabled elemental mapping of the catalyst. High-resolution transmission electron microscopy (HR- TEM, FEI USA, Tecnai G2 20) has been employed to evaluate the orientation of $BaTiO_3$ over stacked rGO sheets. Fourier transform infrared spectroscopy (FTIR, PerkinElmer, USA) and UV-vis diffuse reflectance spectra (DRS, PerkinElmer spectrometer) aided in elucidation of nature of participating bonds and absorbance of light in samples respectively. The photoluminescence (PL) spectrum was recorded by Agilent Technologies (Carry eclipse) equipment under 380 nm excitation.

2.4. Performance assessment of the catalyst. RhB (10 ppm, 30 mL) has been used to assess the performance of the catalyst with respect to various oxidation processes. MO (10ppm, 30mL) has been employed to investigate the effect of pH on the activity of the composites. Aqueous suspensions of both dyes were subjected to magnetic stirring under dark for 90 minutes prior to irradiation, to attain the adsorption-desorption equilibrium. Subsequently, 15mg of composite was immersed into vessels containing 10ppm (30 mL) solution of RhB and MO respectively and has been subjected to continuous and vigorous stirring under dark. A 150 W halogen lamp (with UV cut off filter $\lambda \geq 400$nm) was used for irradiation, held perpendicularly at a distance of 20 cm from the experimental setup. UV-visible spectrophotometer (Shimadzu UV) assisted in monitoring the change in the concentration gradient of the dyes accounting for multiple oxidation processes. The sonocatalytic and sonophotocatalytic degradation mechanism was investigated using an ultrasonic bath (XUB6) with frequency of 35 kHz and 200W power. To affirm reproducibility and reusability, several iterations were performed for the same batch of composites. It could be concluded that catalyst performance is invariant to repetitive iterations.

3. Results and discussions

3.1. Computational investigations. The optimized structure of $BaTiO_3$ with its reciprocal lattice as pseudopotential representation exhibiting Brillouin zone, is shown in figure 2 (a). Figure 2 (b) shows the projected DOS for $BaTiO_3$.The peaks observed below the Fermi level (E_f) at approximately 16 eV, 10 eV and 4 eV correspond to O-2s, Ba-5p and O-2p orbitals, respectively. The contribution of different orbitals can be observed near the Fermi level (0 eV), E_f. However, major contributions originate from the O-2s states and Ti-3d states. The valence band is majorly constituted of O-2p states and Ti-3dorbitaldominates the conduction band. DOS further offers a valuable insight which helps to elucidate the nature of contact between the Ti-3d and O-2p states and hence the electronic structure. In addition, from figure 2(b) the overlap of Ti-3d and O-2p states can be seen, which is associated with the covalency manifesting between these states. Figure 2 (c) shows the total DOS for $BaTiO_3$ lattice. As evaluated by CASTEP, the difference between the Ti-3d valence states and O-2p conduction states contributes to a band gap of 1.81eV at the Γ point. Figure 2(d) shows the optimized geometry of the $BaTiO_3$-rGOcomposite with its Brillouin zone. The contribution of orbitals in the composite structure can be elucidated by projected DOS of the geometry, see figure 2 (e). A conventional "U-shaped profile" at E_f can be observed in the projected DOS structure of the composite. The redistribution of energies and interaction due to rGO and barium titanate causes a slight shift of 0.7 and 0.4 eV in the O-2p and Ti-3d states respectively. Thus, it has been deduced that rGO is not involved in band-gap modification. A predominant localisation of electronic charge around the 2p states of O and C, contributing majorly towards valence band, can be observed. Additionally the valence band maximum is partially occupied by Ti-3d owing to the interfacial charge transfer from rGO to $BaTiO_3$. Conduction band minimum state largely comprise of Ti-3d orbitals and partly 2p orbitals from rGO. On interfacing the perovskite with rGO, visible light absorption involves transitions between high lying valence band states and low lying conduction states. The visible light irradiation

causes electrons to be directly excited into Ti-3d orbitals which form the predominant electron-density component of the low lying conduction band states. The total DOS of $BaTiO_3$-rGOcomposite, as in figure 2 (f), shows the contribution of all the states involved and corresponds to the peaks of projected DOS. It is well established that LDA approach underestimates the band gap for both semiconductors and insulators due to self-interaction error of electrons and inadequacy of derivative discontinuity[27, 28]. The scissor operator of 1.76 eV can be employed to adjust the theoretical band gap with experimentally evaluated band gap**.** Further details have been reported in section S1 of the supporting information.

3.2. Structure of the catalyst and characterization. The XRD pattern for rGO, pure $BaTiO_3$ and $BaTiO_3$-rGO composites (10% rGO) has been shown in figure 3(a). The observed peak splitting at approximately (2θ=) 45° in the XRD pattern for $BaTiO_3$ corresponds to the tetragonal $BaTiO_3$ phase (JCPDS No. 01-075-0583) with lattice parameters of a = b= 3.9950 Å, c = 4.0340 Å. The diffraction peaks at (2θ=) 22.29°, 31.53°, 38.92°, 45.06/45.31°, 50.87°, 56.34°, 65.93°, 70.48°, 75.03° and 79.44° account for the Bragg reflections from the <100>, <110>, <111>, <002>/<200>, <102>, <211>, <220>, <212>, <310> and <311> planes respectively. Due to the low mass concentration of rGO, its weak diffraction intensity and the stack disorder due to intercalation of $BaTiO_3$ particles[29],no diffraction peaks of rGO could be observed in acquired XRD pattern of $BaTiO_3$-rGOcomposite. The results also indicate that decorating $BaTiO_3$ particles on the rGO sheets does not affect the phase of particles.

PL emission spectra as shown in figure 3 (b), aided in investigating the separation efficiency of photogenerated electrons and holes and the excited state of the catalysts under consideration. The peak of $BaTiO_3$at 392 nm has been quenched in the composites. This is further accompanied by decrease in the emission efficiency and is indicative of significant reduction of the electron-hole combination of the composite. This can be accredited to the interfacial transfer from the surface of excited catalyst[30, 31]. Most advanced oxidation

processes are governed by participation of unstable active charged species. Therefore, the proposed catalyst enhances their participation by improving interfacial charge transfer process, inhibiting charge neutralization and prolonging the lifetime for photo-generated charge carrier species.

Figure 3(c) exhibits the FTIR spectra of GO and its composites which confirms the conversion of GO to rGO. In FTIR spectra of GO, characteristic peaks at 3406 cm^{-1} correspond to O–H stretching, 1720 cm^{-1} to C=O stretching and 1625 cm^{-1} can be attributed to skeletal vibrations of unoxidized graphitic domains. The peak at 1403 cm^{-1} corresponds to O–H deformation, and the peak at 1234 cm^{-1}corresponds to C–OH stretching[32]. FTIR spectra of the $BaTiO_3$ – rGO composite confirms the formation of rGO, as the oxygen containing functional groups have been almost diminished in the spectra. The peak at 541 cm^{-1} is due to vibration of Ti-O bond and the peak at 1437 cm^{-1} is related with CO_3^{2-} impurities from barium carbonate[33].

The optical properties of the pristine $BaTiO_3$ particles (without rGO) and the composites have been examined by using UV−Vis diffuse reflectance spectra (Figure 3(d)). The absorption edge of the $BaTiO_3$-rGO composites remains same as pristine particles, which indicates that the band gap is not affected. However, the absorption intensity increases for the composites, which can be attributed to the rearrangement of energy levels of $BaTiO_3$. This increase of absorption efficiency also indicates the potential of the composite to utilize the visible light irradiation efficiently.

3.3. Surface morphology of the catalyst. Figure 4 (a) shows an SEM micrograph for pristine $BaTiO_3$ particles. The average size of $BaTiO_3$ particles is ~60-70 nm. Figure 4(b) is a SEM micrograph for $BaTiO_3$-rGO composites. It can be observed that hydrothermal synthesis does not affect the grain size of $BaTiO_3$ particles. In addition, the morphology of $BaTiO_3$ particles anchored onto the stacked layers of rGO sheets can be observed. Figure 4(c) shows the EDX

analysis of $BaTiO_3$ particles, where peaks of Ba, Ti and O can be observed. No trace of external impurities could be detected within the resolving capacity of EDX, indicating the purity of fabricated catalyst. Additional peaks in the EDX analysis of carbon have been detected in $BaTiO_3$-rGOnanocomposite, presented in figure 4(d),exhibits the presence of graphene in the composites.

TEM microscopy further confirms the morphology of composite as seen in figure5 (a). $BaTiO_3$ particles are observed to be thoroughly anchored to the stacked layers of rGO. TEM also aided in determining the size and orientation of $BaTiO_3$ particles. Figure 5(b) demonstrates selected area electron diffraction (SAED) of composites. The crystalline nature of the $BaTiO_3$ particles is indicated by the presence of dark spots in the micrograph which correspond to diffraction from a single crystal. The zone axis can be further identified for these patterns. Reflection from the $(20\bar{2})$ and $(\bar{2}20)$ planes relate to the first two spots in the pattern respectively. Considering orientation from the (111) plane, these planes are associated with the tetragonal structure.

3.4. Performance evaluation of the composite through advanced oxidation processes. RhB has been used as a standard organic contaminant to evaluate the key operating conditions and performance of the $BaTiO_3$-rGOcomposites with respect to various oxidation processes. It is imperative to determine the adsorption capacity of the composites under consideration for RhB, as the degradation is significantly dependent on it. The adsorption investigations revealed that degradation profile follows a Langmuir pseudo-second order model. The equilibrium adsorption capacity (q_e)and adsorption rate constant (k_{ads}) were determined to be 33.2 $mg/g_{catalyst}$and 3.7 x 10^{-5}g/mg-min, respectively (supporting information, S2). The photocatalytic, sonocatalytic and sonophotocatalytic degradation of RhB was governed by Langmuir-Hinshelwood model(supporting information, S2).Figure 6 (a) shows the second order kinetic plot for the adsorption of RhB on the composites and figure 6 (b) is a linear

transform $\ln(C/C_0)$ as a function of time corresponding to sonocatalytic, photocatalytic and sonophotocatalytic degradation, respectively. The results followed a pseudo first order reaction and the reaction rate has been determined as 0.036 min^{-1}, 0.055 min^{-1} and 0.09935 min^{-1} for sonocatalytic, photocatalytic and sonophotocatalytic degradation, respectively. The reaction rates are comparable and even higher than those reported for multiple hybrid catalysts[34-36].

Upon careful assessment of degradation profiles following deductions can be made abou t individual processes and their hybridization: (i)RhB degradation (photolysis)is negligible under visible light irradiation and in the presence of pristine $BaTiO_3$ particles (supporting information, S2)(ii)significant degradation of RhB (in presence of the composites) was accomplished within a span of 90 minutes; this is credited to surface adsorption of dye (iii) prominent degradation of RhB is achieved under visible light irradiation; attributable to reduced recombination of photo-induced electron-hole pairs upon delocalization of electrons over rGO. This phenomenon is associated with rGO's ability to act as macromolecular sensitizer for perovskite and the Schotky-barrier effect which in turn significantly improves the lifetime of generated electron-hole pairs; thereby improving the utilization of charge carriers for degradation of the organic pollutant (iv) ultrasonic treatment assisted in surface adsorption hence, leading to better dye degradation. This can be explained in terms of system response under acoustic waves, where two major parameters come into play. Primarily, sonication induces cavitation and the implosion of cavitation bubbles provides extremely localized supercritical conditions of high temperature, high pressure, electrical discharges and plasma effects. This leads to cleavage of dissolved oxygen and water molecules and ultimately forms participating radicals. Thereafter, these radicals react with the target pollutant molecule and accelerate their decomposition.

Secondly, multi-bubble sonoluminescence also governs the process of dye mineralization. This can be ascribed to the emission of photons resulting from collapsing bubbles, driven by acoustic energy. Subsequently, these photons trigger the excitation of electrons which improves the participation of charge carriers. Other factors contributing towards enhanced degradation of the contaminants are de-agglomeration of the catalytic compound and mass transfer of the reactants. The characteristic stern layer formation in $BaTiO_3$ allows effective curbing of electron-hole neutralization, making it a perfect choice for a catalyst. Additionally, coupling of an acoustic effect and the piezoelectric nature of $BaTiO_3$ contributes to piezophototronic effect whichfurther ameliorates the overall performance[37].

Hence, synergistic effects arising due to hybridization of sonocatalysis and photocatalysis in presence of $BaTiO_3$-rGO composites is highly desirable in efficient degradation of targeted dye pollutants.

3.5. Effect of pH. In order to evaluate the effect of pH on the performance of the composite, the change in rate of MO degradation rate was considered. On varying the pH a maximum degradation rate of MO, through the composites, was observed in the acidic region(red form, pH 3).In addition, Liu et al.[38] reported a pH value of 3 to be optimal for maximum photocatalytic decomposition of MO. However, the underlying principles for enhanced performance contributing towards decomposition of the red form of MO are not yet clearly established. This phenomenon is due to the fact that in an acidic medium, a hydrogen ion is attracted by nitrogen. This induces a delocalization of the positive charge over the structure, arising from the movement of the lone pair of electrons. The absorption shifts to longer wavelengths or lower frequencies, as the delocalization increases. Since absorbance at pH 3 corresponds to a highly delocalized structure of MO[38, 39],it has been used to analyze the performance of composite.

Figure7 (a) demonstrates the pseudo first order kinetic plot for adsorption of MO over the composites. Slope of the plot accounts for equilibrium adsorption capacity (q_e) and has been

299 determined to be 32.7 mg/$g_{catalyst}$. The adsorption rate constant (k_{ads}) is given by the intercept,
300 which is found to be 2.3 x 10^{-5}g/mg-min (Supporting information, S3).
301 Figure 7 (b) shows the linear transform for kinetic curve corresponding to pseudo first order
302 reaction.The reaction rate constant were 0.0133 min^{-1} , 0.0138 min^{-1} and 0.01587 min^{-1} for
303 sonocatalytic, photocatalytic and sonophotocatalytic degradation respectively (Supporting
304 information, S3).
305 The schematic in figure 8 indicates the proposed photocatalytic and sonophotocatalytic
306 mechanism employing barium titanate particles decorated over rGO sheets, also
307 demonstrating the underlying mechanism for formation of the delocalised structure of MO.
308 Figure 9 (a) exhibits the comparative degradation (%) of RhB through surface adsorption and
309 oxidation processes, plotted as a function of irradiation time. Considering only surface
310 adsorption, the degradation (%) level using the $BaTiO_3$–rGOcompositewas estimated to be
311 61.10 %. The degradation (%) through photocatalytic, sonocatalytic and sonophotocatalytic
312 mechanism was estimated to be82.4%, 72.7% and 97.3 % respectively.

313 A comparison of the degradation (%) of MO through surface adsorption and oxidation
314 processes against irradiation time is shown in figure 9 (b).The observed 59.6% degradation
315 can be attributed to surface adsorption, owing to the porous structure of the composite. The
316 highest degradation of 81.9% was achieved through sonophotocatalysis, followed by 78.2%
317 through photocatalysis and 66.8% through sonocatalysis. Figure 9 (c) exhibits degradation
318 percentage of RhB and MO with respect to different photocatalytic cycle.

319 In order to investigate the degradation mechanism exhibited by the proposed catalysts, it is
320 crucial to study and investigate the energy band potentials (refer section S4 of the
321 supplementary information). It could be established that the active species involved in the
322 degradation are mainly ·OH and H_2O_2.

The cumulative results are indicative of the benefits that synergistic effect accompanies, which plays a vital role in enhancing the performance of the composite for dye degradation.

4. Conclusions

To summarize, a theoretical study utilizing DFT with plane wave total energy sets and pseudopotential approach has been employed to facilitate assimilation at a molecular point of view. Projected and total density of states has aided in determining the nature of electronic coupling and the contribution of orbitals. In addition, DOS assisted in corroborating investigations on energy band potentials in the composites by indicating electron excitation from the valence states to conduction states.

Further, the proposed methodology aims to provide several benefits through effective utilization of multiple advanced oxidation processes. $BaTiO_3$-rGO composites have been prepared via a hydrothermal synthesis route using hydrazine as a reducing agent. The XRD pattern provided details of the phase homogeneity of the composite. The nature, vibrations and oscillations of participating bonds have been evaluated by FTIR. DRS and PL measurements exhibited enhanced light absorption capacity and reduction in charge neutralization, respectively.SEM and HR-TEM revealed that the $BaTiO_3$ particles are firmly anchored on the stacked layers of rGO. Stacked sheets of rGO not only acted as electron reservoir, but also as a photosensitizer for $BaTiO_3$ particles. This facilitated trapping and scavenging of the injected electrons in the conduction band of the perovskite which is subsequently followed by radical reactions. MO was used as targeted dye contaminant to probe the effect of pH on degradation mechanism. The results indicate that $BaTiO_3$–rGO composites provide a route for efficient, green, sustainable and cost-effective detoxification.

Author Information

*Email:rahul@iitmandi.ac.in

Notes:

The authors declare no competing financial interests.

Acknowledgements

RV thanks Indian National Science Academy, New Delhi, India for financial support under INSA Young Scientists Scheme.The support of Materials Research Centre (MRC), University of Bath and Advanced Materials Research Centre (AMRC) atIIT Mandi, is also being acknowledged.

Supporting Information

This article carries information on CASTEP convergencecorresponding to the optimized structure of the nanocomposites. The supplementary data also covers degradation profile of RhB and MO corresponding to adsorption, photocatalysis, sonocatalysis and sonophotocatalysis. Further, the kinetics accounting for degradation of both the dyes, has also been discussed.

References

[1] Y. Cui, J. Briscoe, S. Dunn, Effect of Ferroelectricity on Solar-Light-Driven Photocatalytic Activity of BaTiO3 瑕 Influence on the Carrier Separation and Stern Layer Formation, Chemistry of Materials 25(21) (2013) 4215-4223.

[2] Q. Xiang, J. Yu, M. Jaroniec, Graphene-based semiconductor photocatalysts, Chemical Society Reviews 41(2) (2012) 782-796.

[3] Z.W. Seh, S. Liu, M. Low, S.Y. Zhang, Z. Liu, A. Mlayah, M.Y. Han, Janus Au-TiO2 Photocatalysts with Strong Localization of Plasmonic Near-Fields for Efficient Visible-Light Hydrogen Generation, Advanced Materials 24(17) (2012) 2310-2314.

[4] P.V. Kamat, Graphene-based nanoassemblies for energy conversion, The Journal of Physical Chemistry Letters 2(3) (2011) 242-251.

[5] C. Huang, C. Li, G. Shi, Graphene based catalysts, Energy & Environmental Science 5(10) (2012) 8848-8868.

[6] W. Fan, Q. Lai, Q. Zhang, Y. Wang, Nanocomposites of TiO2 and reduced graphene oxide as efficient photocatalysts for hydrogen evolution, The Journal of Physical Chemistry C 115(21) (2011) 10694-10701.

[7] G. Williams, B. Seger, P.V. Kamat, TiO2-graphene nanocomposites. UV-assisted photocatalytic reduction of graphene oxide, ACS nano 2(7) (2008) 1487-1491.

[8] Y. Zhang, N. Zhang, Z.-R. Tang, Y.-J. Xu, Graphene transforms wide band gap ZnS to a visible light photocatalyst. The new role of graphene as a macromolecular photosensitizer, ACS nano 6(11) (2012) 9777-9789.
[9] Z. Xiong, L.L. Zhang, J. Ma, X. Zhao, Photocatalytic degradation of dyes over graphene–gold nanocomposites under visible light irradiation, Chemical Communications 46(33) (2010) 6099-6101.
[10] R.-X. Wang, Q. Zhu, W.-S. Wang, C.-M. Fan, A.-W. Xu, BaTiO 3–graphene nanocomposites: synthesis and visible light photocatalytic activity, New Journal of Chemistry (2015).
[11] S. Gupta, V. Subramanian, Encapsulating Bi2Ti2O7 (BTO) with reduced graphene oxide (RGO): an effective strategy to enhance photocatalytic and photoelectrocatalytic activity of BTO, ACS applied materials & interfaces 6(21) (2014) 18597-18608.
[12] P. Ren, H. Fan, X. Wang, Solid-state synthesis of Bi2O3/BaTiO3 heterostructure: preparation and photocatalytic degradation of methyl orange, Applied Physics A 111(4) (2013) 1139-1145.
[13] N. Song, H. Fan, H. Tian, Reduced graphene oxide/ZnO nanohybrids: Metallic Zn powder induced one-step synthesis for enhanced photocurrent and photocatalytic response, Applied Surface Science 353 (2015) 580-587.
[14] N. Song, H. Fan, H. Tian, PVP assisted in situ synthesis of functionalized graphene/ZnO (FGZnO) nanohybrids with enhanced gas-sensing property, Journal of Materials Science 50(5) (2015) 2229-2238.
[15] M. Rastogi, H. Kushwaha, R. Vaish, Highly efficient visible light mediated azo dye degradation through barium titanate decorated reduced graphene oxide sheets, Electronic Materials Letters 12(2) (2016) 281-289.
[16] A. Lucid, A. Iwaszuk, M. Nolan, A first principles investigation of Bi 2 O 3-modified TiO 2 for visible light Activated photocatalysis: The role of TiO 2 crystal form and the Bi 3+ stereochemical lone pair, Materials Science in Semiconductor Processing 25 (2014) 59-67.
[17] C.G. Joseph, G.L. Puma, A. Bono, D. Krishnaiah, Sonophotocatalysis in advanced oxidation process: a short review, Ultrasonics Sonochemistry 16(5) (2009) 583-589.
[18] S.J. Clark, M.D. Segall, C.J. Pickard, P.J. Hasnip, M.I. Probert, K. Refson, M.C. Payne, First principles methods using CASTEP, Zeitschrift für Kristallographie 220(5/6/2005) (2005) 567-570.
[19] J.P. Perdew, M. Levy, Physical content of the exact Kohn-Sham orbital energies: band gaps and derivative discontinuities, Physical Review Letters 51(20) (1983) 1884.
[20] M. Grüning, A. Marini, A. Rubio, Density functionals from many-body perturbation theory: The band gap for semiconductors and insulators, The Journal of chemical physics 124(15) (2006) 154108.
[21] R. Jose, N.U. Zhanpeisov, H. Fukumura, Y. Baba, M. Ishikawa, Structure-property correlation of CdSe clusters using experimental results and first-principles DFT calculations, Journal of the American Chemical Society 128(2) (2006) 629-636.
[22] C. Dong, X. Li, J. Qi, First-principles investigation on electronic properties of quantum dot-sensitized solar cells based on anatase TiO2 nanotubes, The Journal of Physical Chemistry C 115(41) (2011) 20307-20315.
[23] T. Albaret, F. Finocchi, C. Noguera, Density functional study of stoichiometric and O-rich titanium oxygen clusters, The Journal of Chemical Physics 113(6) (2000) 2238-2249.
[24] Z.-w. Qu, G.-J. Kroes, Theoretical study of the electronic structure and stability of titanium dioxide clusters (TiO2) n with n= 1-9, The Journal of Physical Chemistry B 110(18) (2006) 8998-9007.
[25] W. Geng, H. Liu, X. Yao, Enhanced photocatalytic properties of titania–graphene nanocomposites: a density functional theory study, Physical Chemistry Chemical Physics 15(16) (2013) 6025-6033.
[26] T. Chen, B. Zeng, J. Liu, J. Dong, X. Liu, Z. Wu, X. Yang, Z. Li, High throughput exfoliation of graphene oxide from expanded graphite with assistance of strong oxidant in modified Hummers method, Journal of Physics: Conference Series, IOP Publishing, 2009, p. 012051.
[27] B.M. II, J. Autschbach, Longest-Wavelength Electronic Excitations of Linear Cyanines: The Role of Electron Delocalization and of Approximations in Time-Dependent Density Functional Theory, Journal of Chemical Theory and Computation 9(11) (2013) 4991-5003.

[28] V.N. Staroverov, G.E. Scuseria, J. Tao, J.P. Perdew, Comparative assessment of a new nonempirical density functional: Molecules and hydrogen-bonded complexes, The Journal of chemical physics 119(23) (2003) 12129-12137.
[29] T. Xian, H. Yang, L. Di, J. Ma, H. Zhang, J. Dai, Photocatalytic reduction synthesis of SrTiO3-graphene nanocomposites and their enhanced photocatalytic activity, Nanoscale research letters 9(1) (2014) 1-9.
[30] K. Zhou, Y. Zhu, X. Yang, X. Jiang, C. Li, Preparation of graphene–TiO 2 composites with enhanced photocatalytic activity, New Journal of Chemistry 35(2) (2011) 353-359.
[31] G. Liao, S. Chen, X. Quan, H. Yu, H. Zhao, Graphene oxide modified gC 3 N 4 hybrid with enhanced photocatalytic capability under visible light irradiation, Journal of Materials Chemistry 22(6) (2012) 2721-2726.
[32] S. Stankovich, R.D. Piner, S.T. Nguyen, R.S. Ruoff, Synthesis and exfoliation of isocyanate-treated graphene oxide nanoplatelets, Carbon 44(15) (2006) 3342-3347.
[33] H. Reverón, C. Aymonier, A. Loppinet-Serani, C. Elissalde, M. Maglione, F. Cansell, Single-step synthesis of well-crystallized and pure barium titanate nanoparticles in supercritical fluids, Nanotechnology 16(8) (2005) 1137.
[34] S. Liu, X. Chen, X. Chen, A TiO 2/AC composite photocatalyst with high activity and easy separation prepared by a hydrothermal method, Journal of hazardous materials 143(1) (2007) 257-263.
[35] R. Ullah, J. Dutta, Photocatalytic degradation of organic dyes with manganese-doped ZnO nanoparticles, Journal of hazardous materials 156(1) (2008) 194-200.
[36] B. Tryba, Immobilization of TiO 2 and Fe–C–TiO 2 photocatalysts on the cotton material for application in a flow photocatalytic reactor for decomposition of phenol in water, Journal of hazardous materials 151(2) (2008) 623-627.
[37] H. Li, Y. Sang, S. Chang, X. Huang, Y. Zhang, R. Yang, H. Jiang, H. Liu, Z.L. Wang, Enhanced Ferroelectric-Nanocrystal-Based Hybrid Photocatalysis by Ultrasonic-Wave-Generated Piezophototronic Effect, Nano letters 15(4) (2015) 2372-2379.
[38] J. Liu, Y. Sun, Z. Li, Ag loaded flower-like BaTiO 3 nanotube arrays: Fabrication and enhanced photocatalytic property, CrystEngComm 14(4) (2012) 1473-1478.
[39] H.A. Mourão, O.F. Lopes, C. Ribeiro, V.R. Mastelaro, Rapid hydrothermal synthesis and pH-dependent photocatalysis of strontium titanate microspheres, Materials Science in Semiconductor Processing 30 (2015) 651-657.

Figure captions:

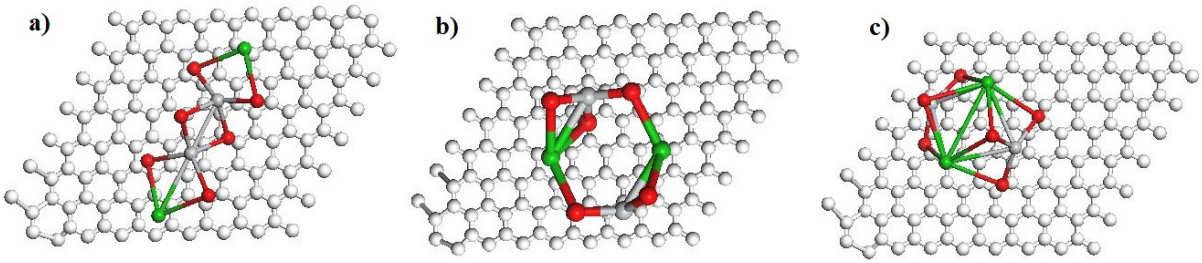

Figure 1: Optimized geometries of the composite with possible isomers of graphene oxide with $(BaTiO_3)_2$ clusters. White, gray, red and green spheres stand for C, Ti, O and Ba, respectively.

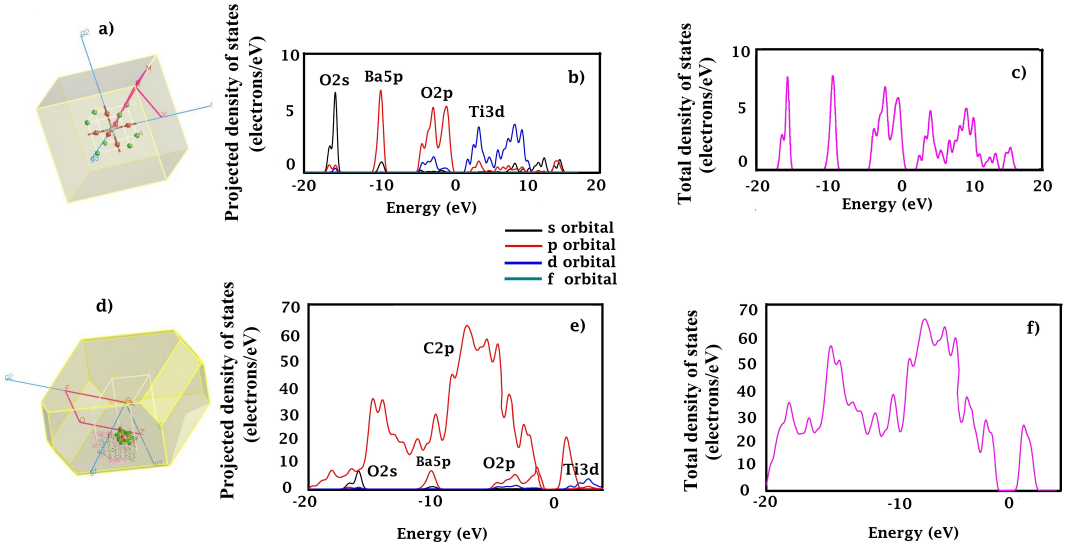

Figure 2: (a) Optimized geometry with cubic Brillouin zone representation (b) projected DOS of $BaTiO_3$ and (c) total DOS of $BaTiO_3$ (d) optimized geometry with triclinic Brillouin Zone representation (e) projected DOS of $BaTiO_3$-rGOand (f) total DOS of $BaTiO_3$-rGO.

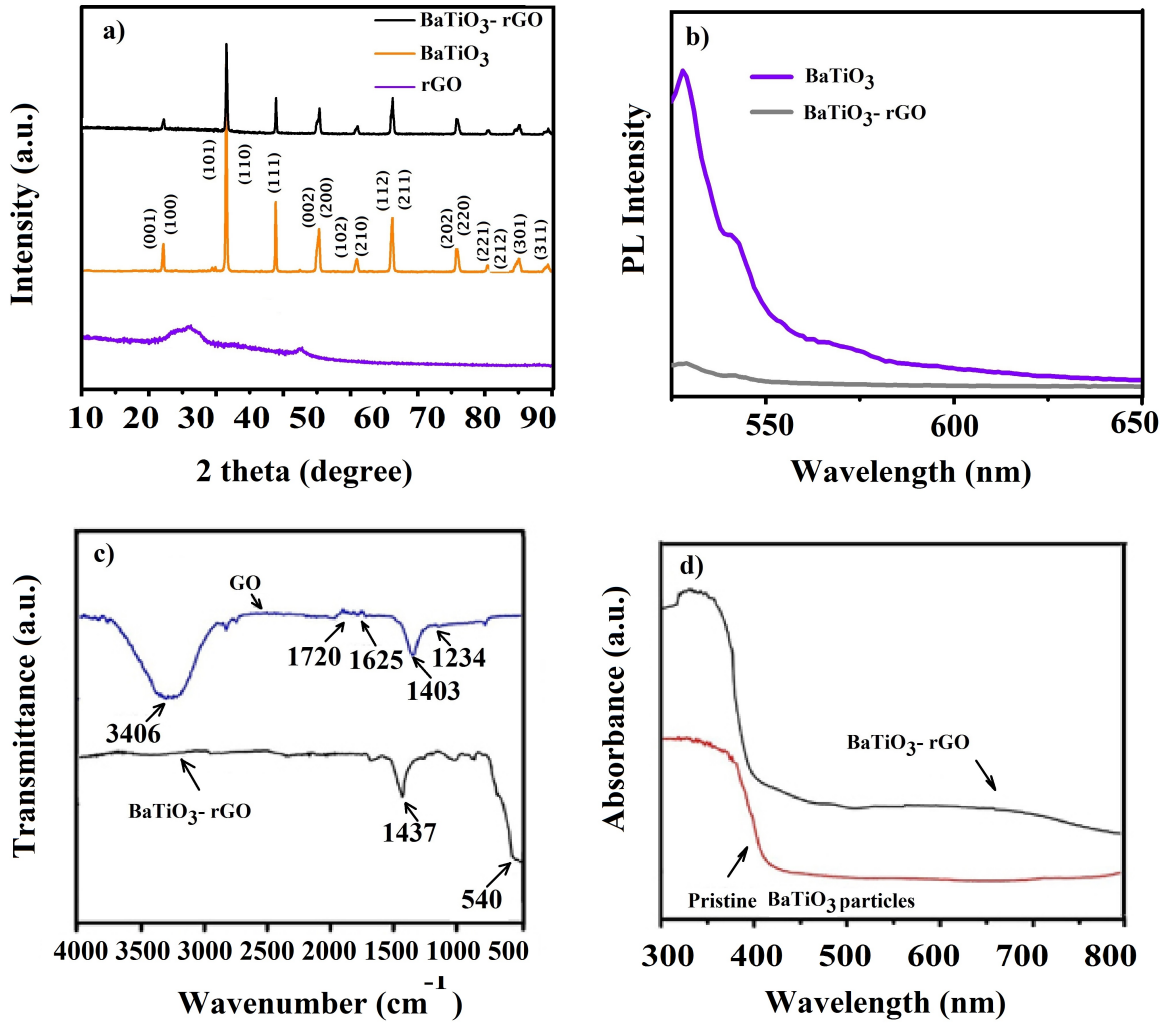

480

481 **Figure3:**(a) XRD pattern for $BaTiO_3$-rGOcomposite, $BaTiO_3$ and rGO, (b) PL spectrum for

482 pristine $BaTiO_3$ particles and composite (c) DRS pattern and (d) FTIR for $BaTiO_3$ – rGO

483 composite and pristine $BaTiO_3$ particles.

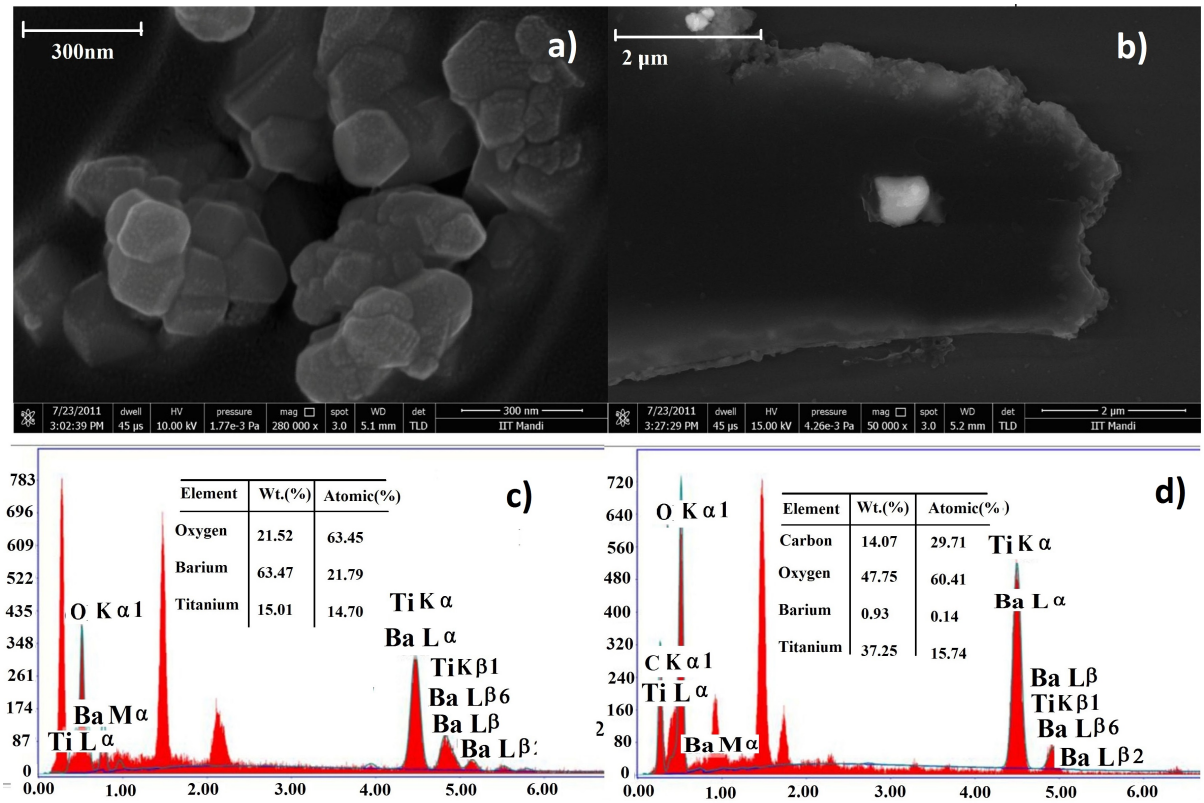

Figure 4: (a) SEM micrograph of pristine $BaTiO_3$ particles (b) SEM micrograph showing $BaTiO_3$ particles decorated on stacked sheets of reduced graphene oxide in the $BaTiO_3$ – rGO composite (c) EDX of $BaTiO_3$ and (d) EDX of $BaTiO_3$-rGO composite showing peaks, weight and atomic percent of the involved elements.

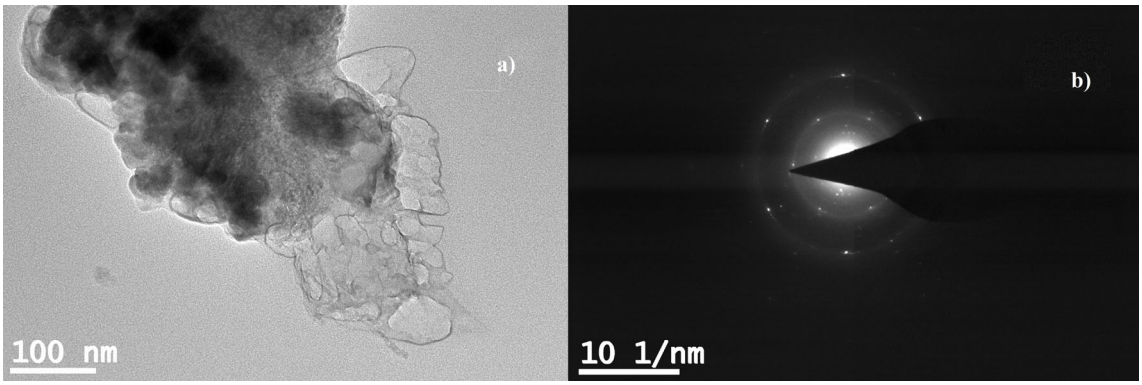

Figure 5: (a) TEM micrograph of the $BaTiO_3$-rGO composite (b) SAED pattern of the $BaTiO_3$-rGO composite.

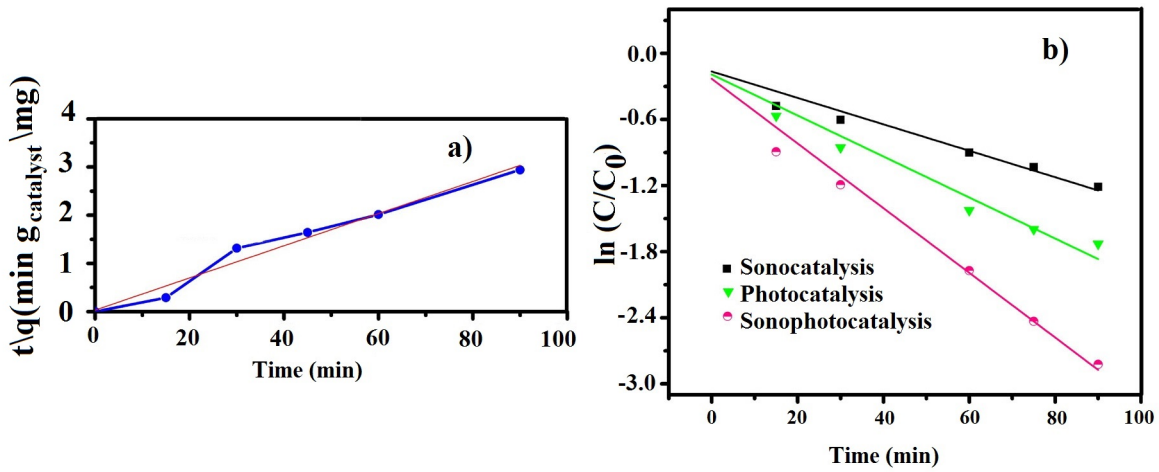

493

494 **Figure 6:**(a) Pseudo-second order kinetic plot for the RhB dye degradation through $BaTiO_3$-
495 rGO composites corresponding to adsorption desorption equilibrium (b) Linear transform of
496 the pseudo first order kinetic curve corresponding to sonocatalytic, photocatalytic and
497 sonophotocatalytic degradation of RhB.

498

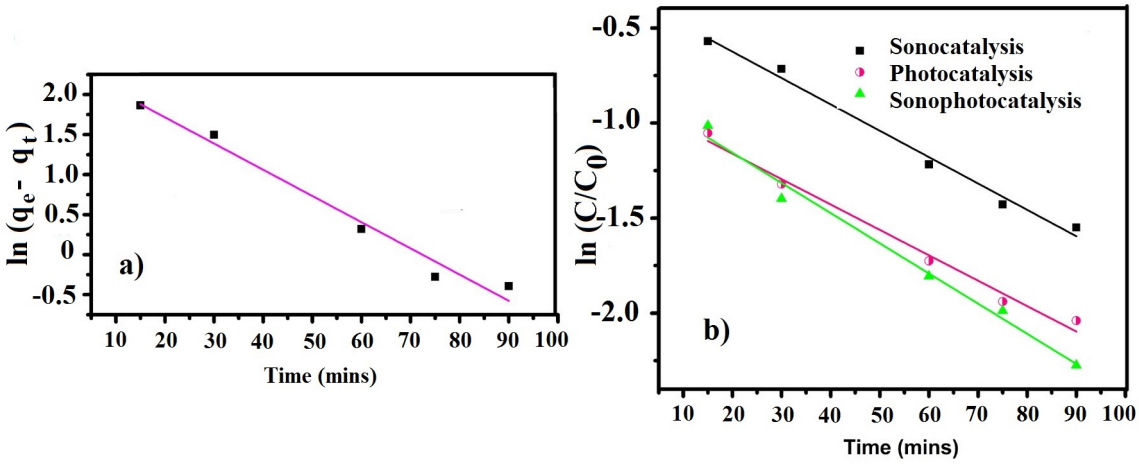

499

500 **Figure 7:**(a) Pseudo-first order kinetic plot for MO adsorption -desorption equilibrium (b)
501 Linear transform of the pseudo first order kinetic curve corresponding to sonocatalytic,
502 photocatalytic and sonophotocatalytic degradation ofMO.

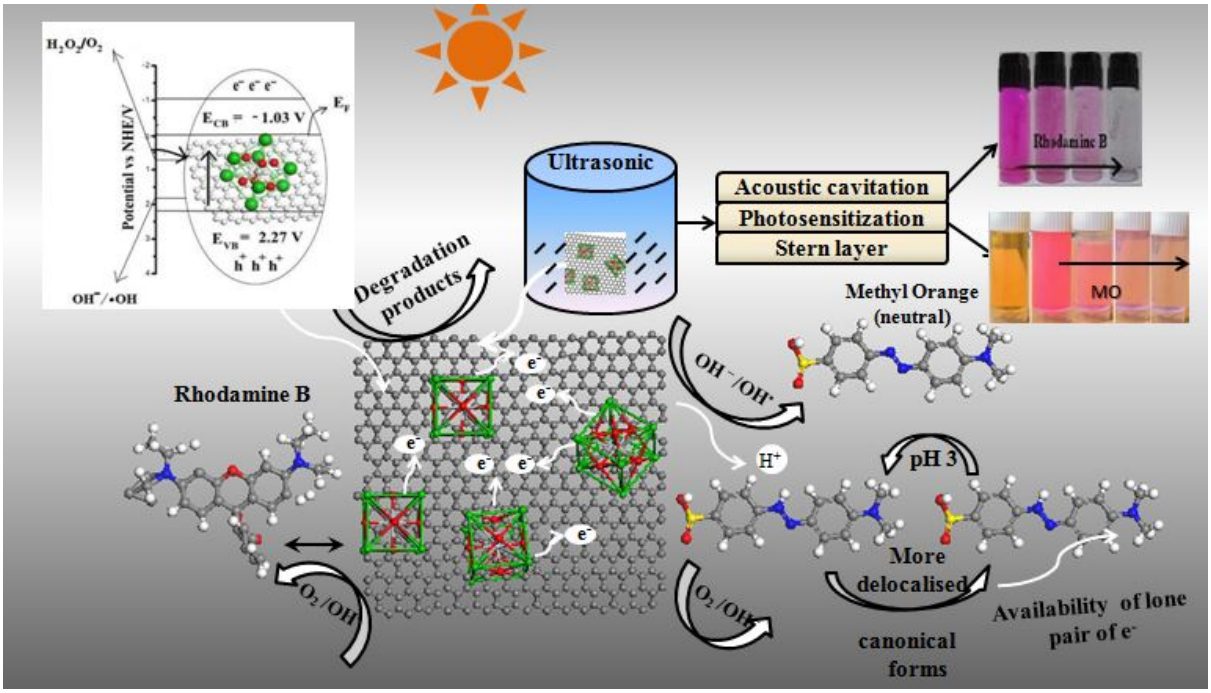

503

504 **Figure 8:** Schematic illustration of the proposed approach (also exhibiting the delocalised

505 structure of MO).

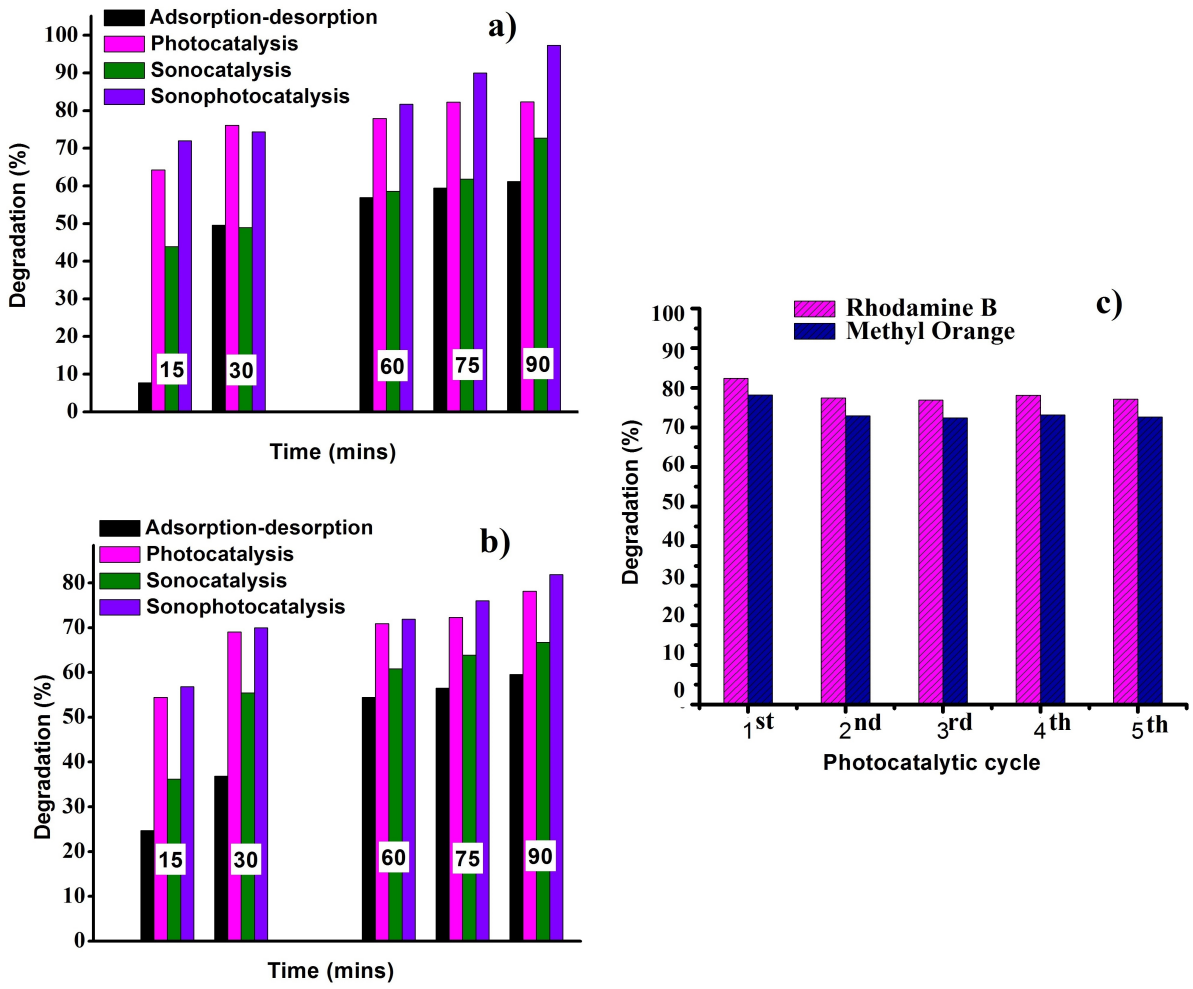

506

507 **Figure 9:**Comparison of degradation percentage vs. irradiation time for a) RhB and b) MO
508 with respect to adsorption- desorption and various oxidation processes for the composite c)
509 degradation percentage of RhB and MO with respect to different photocatalytic cycle.